# Is Bursting More Effective than Spiking in Evoking Pituitary Hormone Secretion? A Spatiotemporal Simulation Study of Calcium and Granule Dynamics

Alessia Tagliavini[1], Joël Tabak[2,3], Richard Bertram[2], Morten Gram Pedersen[1]

[1] Department of Information Engineering, University of Padua, Padua, Italy

[2] Department of Mathematics and Program in Neuroscience and Molecular Biophysics, Florida State University, Tallahassee, FL 32306, USA

[3] Exeter University Medical School, Biomedical Neuroscience, Exeter, UK

Corresponding author:

Morten Gram Pedersen,

Department of Information Engineering, University of Padua,

Via Gradenigo 6/B, 35131 Padua, Italy.

Email: pedersen@dei.unipd.it

Running head:

Pituitary secretion evoked by bursting and spiking

Author contributions:

Conceived research: RB, MGP

Performed research: AT, JT

Prepared figures: AT

Wrote and edited manuscript, and approved final version: AT, JT, RB, MGP

Keywords: electrical activity; exocytosis; $Ca^{2+}$ oscillations; mathematical modeling; dynamic clamp.

**ABSTRACT**

Endocrine cells of the pituitary gland secrete a number of hormones, and the amount of hormone released by a cell is controlled in large part by the cell's electrical activity and subsequent $Ca^{2+}$ influx. Typical electrical behaviors of pituitary cells include continuous spiking and so-called pseudo-plateau bursting. It has been shown that the amplitude of $Ca^{2+}$ fluctuations is greater in bursting cells, leading to the hypothesis that bursting cells release more hormone than spiking cells. In this work, we apply computer simulations to test this hypothesis. We use experimental recordings of electrical activity as input to mathematical models of $Ca^{2+}$ channel activity, buffered $Ca^{2+}$ diffusion, and $Ca^{2+}$-driven exocytosis. To compare the efficacy of spiking and bursting on the same cell, we pharmacologically block the large conductance potassium (BK) current from a bursting cell, or add a BK current to a spiking cell via dynamic clamp. We find that bursting is generally at least as effective as spiking at evoking hormone release, and is often considerably more effective, even when normalizing to $Ca^{2+}$ influx. Our hybrid experimental/modeling approach confirms that adding a BK-type $K^+$ current, which is typically associated with decreased cell activity and reduced secretion, can actually produce an increase in hormone secretion, as suggested earlier.

## INTRODUCTION

Endocrine cells of the pituitary gland (i.e., melanotrophs, lactotrophs, somatotrophs, thyrotrophs, corticotrophs, and gonadotrophs) secrete a number of hormones and are regulated by the hypothalamus (30). These hormones act on other endocrine glands and other tissues including the brain to regulate physiological and behavioral aspects of growth, metabolism, water balance, and reproduction (7). The endocrine pituitary cells contain a wide variety of ion channels and are electrically excitable, and hormone secretion occurs due to an elevation in the intracellular $Ca^{2+}$ concentration that often accompanies electrical activity (29). Common behaviors of the cells include continuous spiking – typically observed in luteinizing hormone-secreting gonadotrophs under basal conditions – and a form of bursting known as pseudo-plateau bursting often observed in prolactin-secreting lactotrophs, growth hormone-releasing somatotrophs, and ACTH-secreting corticotrophs, where the burst duration is at most a few seconds and the spikes that ride on the elevated voltage plateau are very small (9, 10). Each electrical event brings $Ca^{2+}$ into the cell, and this $Ca^{2+}$ is responsible for exocytosis of hormone-filled granules. Simultaneous measurements of both electrical activity and $Ca^{2+}$ concentration have established that the amplitude of $Ca^{2+}$ fluctuations is greater in a bursting cell than in a spiking cell (30) leading to the hypothesis that bursting cells release more hormone than spiking cells (8, 9). Experimentally exploring this hypothesis will require simultaneous measurements of electrical activity and release from single cells. The aim of this report is to use computer simulations to explore the hypothesis that pseudo-plateau bursting evokes more secretion than continuous spiking.

The approach that we use is to directly measure electrical spiking and bursting patterns from pituitary cells and use these data as input to mathematical models of $Ca^{2+}$ channel activity, $Ca^{2+}$ diffusion and binding to buffer, and finally $Ca^{2+}$-driven exocytosis. The model parameters are set according to prior data and models, but one major unknown factor is the geometrical arrangement of $Ca^{2+}$ channels and docked granules at the plasma membrane. We consider the secretion response to stochastic single channels as well as small clusters of stochastic channels, and vary the distance of the channels from the release sites. Our objective is to determine how these factors affect the differential secretion evoked by spiking electrical activity vs. bursting electrical activity.

We find that bursting is typically more effective at evoking secretion than is continuous spiking. When bursting is induced in a spiking gonadotroph by injecting a BK-type $K^+$ current with dynamic clamp, our model simulations suggest that the burst pattern is generally at least as effective as continuous spiking at evoking hormone release, and is often considerably more effective. We demonstrate that the degree of superiority of bursting over spiking depends on the channel configuration, which would likely vary from cell-to-cell. We also demonstrate that the bursting reappearing in an endogenously bursting pituitary cell, after previously pharmacologically blocking the native BK current and subsequently adding a BK current using dynamic clamp, is superior at evoking secretion than the pharmacologically induced spiking behavior. Thus, we demonstrate with this hybrid experimental/modeling approach that adding a $K^+$ current, which is typically associated with decreased cell activity and reduced secretion, can actually produce an increase in hormone secretion, as suggested earlier (9).

## METHODS

The inputs to our mathematical models are voltage time courses recorded from a rat gonadotroph or from a GH4C1 lacto-somatotroph cell. We use traces consisting of continuous spiking patterns, and traces of fast pseudo-plateau bursting caused by adding a BK-type current to a spiking cell with the dynamic clamp technique. Each of these traces is fed into a mathematical model consisting of stochastic $Ca^{2+}$ channels coupled to reaction-diffusion equations that describe $Ca^{2+}$ transport through the cell. Finally, the computed $Ca^{2+}$ concentration is used to drive an exocytosis model based on $Ca^{2+}$ binding to granules, granule fusion with the membrane, and resulting hormone release.

### EXPERIMENTAL

GH4C1 cells were maintained in culture conditions in supplemented F10 medium (Sigma-Aldrich, St-Louis, MO) according to established procedures (35). Primary pituitary cells were obtained from diestrous female rats (Sprague Dawley, aged 3-6 months) using enzymatic dispersion of pituitary fragments (33). Animal procedures were approved by the Florida State

University Animal Care and Use Committee. Cells were cultured in supplemented M199 medium (Invitrogen, Carlsbad, CA) for one day before being used for patch clamp experiments. Gonadotrophs were identified by their larger size and by their typical rhythmic hyperpolarizations in response to 1 nM gonadotropin-releasing hormone (Bachem, Torrance, CA) applied at the end of the experiment (38).

During the patch-clamp experiments, cells were superfused with Hepes-buffered saline (138 mM NaCl, 5mM KCl, 10 mM D-glucose, 25 mM HEPES, 0.7 mM $Na_2HPO_4$, 1 mM $MgCl_2$, 2 mM $CaCl_2$) at room temperature. Patch pipettes (resistance 6-9 MOhm) were filled with solution containing 90 mM KAsp, 60 mM KCl, 10 mM HEPES, 1 mM $MgCl_2$ with the addition of 120 g/ml amphotericin B. Usually, access resistance decreased below 50 MOhm within 10 minutes following seal (> 5 GOhm) formation. BK channels were blocked by bath application of 100 nM iberiotoxin (Tocris).

## DYNAMIC CLAMP

Membrane potential was recorded in current clamp (bridge mode) and output from the patch amplifier (Multiclamp 700B, Molecular Devices, Sunnyvale, CA) was read through an analog to digital acquisition card (DAQ) on a PC running the software QuB with a dynamic clamp module (22). Membrane potential ($V$) was used to compute the current going through the BK channels, $I_{BK} = g_{BK} f (V_K - V)$, with $f$ obtained by integrating

$$\tau_{BK} \frac{df}{dt} = f_\infty(V) - f$$

in real time using the forward Euler method (22), with $dt$ average = 54 µs, maximum = 100 µs, and the steady state BK channel activation given by

$$f_\infty(V) = \left[1 + \exp\left((v_f - V)/s_f\right)\right]^{-1} .$$

The calculated BK current was injected back into the cell through the same DAQ. The parameter values were: $g_{BK}$ = 0.5 – 1 nS; $\tau_{BK}$ = 5 – 10 ms; $v_f$ = -15 mV; $s_f$ = 1 mV.

## MODELLING

### GEOMETRY

To model data from pituitary cells we represented a single cell by a sphere with a diameter of 13 μm (5). Based on whole-cell calcium conductance of ~1.5-2 nS (10), and single channel conductance ~20 pS (13), we assumed that a cell possesses 75 functional L-type $Ca^{2+}$ channels. In our simulations we considered two different configurations for the channel distribution over the sphere surface: channels were either uniformly distributed and each release site affected by a single channel, or there were clusters composed of 5 channels, and each release site affected by a single cluster. In the single channel case, $Ca^{2+}$ diffusion was computed in a conical region with base radius of 1.5 μm (Fig. 1a), a radius obtained by dividing the sphere surface into 75 circular areas, one for each channel. This radius corresponds to an inter-channel distance of ~3 μm, in agreement with (11). The single channel conductance was set to 20 pS (13). In the case of channel clusters, $Ca^{2+}$ diffusion was simulated in a conical region with a base radius of 3.3 μm, corresponding to dividing the sphere surface into 15 circular areas. In both cases, the $Ca^{2+}$ current source was located at the base center of the conical region. We implemented no-flux boundary conditions for $Ca^{2+}$ and buffers on the sides of the cone. This assumption means that $Ca^{2+}$ flowing out of the conical region equals the flux into the cone from adjacent regions, or in other words, that the $Ca^{2+}$ channels in adjacent cones contribute to $Ca^{2+}$ levels in the cone of study exactly as the $Ca^{2+}$ channel or cluster under study influences the adjacent regions. Because of the conical geometry, the full 3-dimensional problem was reduced to a 2-dimensional problem, using rotationally symmetric spherical $(r,\theta)$ coordinates, thus reducing the computational requirements. Since the granules participating in hormone secretion are located just below the membrane (14), we focused our attention on the submembrane $Ca^{2+}$ profiles along the plasma membrane.

[Figure 1]

## SINGLE CHANNEL CURRENT

For the single $Ca^{2+}$ channel, we assumed three states with kinetic mechanism described by (28)

$$C \underset{\beta}{\overset{\alpha}{\rightleftharpoons}} O \underset{k_-}{\overset{k_+}{\rightleftharpoons}} B, \tag{1}$$

where the states are closed ($C$), open ($O$), and blocked or inactivated ($B$).

The rate constants $\alpha(V)$ and $\beta(V)$ were determined by $\alpha=m_\infty/\tau_m$ , $\beta=1/\tau_m - \alpha$ (12) using a steady-state activation function $m_\infty$ and time constant $\tau_m$ obtained from experiments. Based on data from GH3 cells (5, 11), which have $Ca^{2+}$ channel characteristics similar to GH4 cells (5), and in agreement with Sherman et al. (28), we set $\tau_m$=1.25 ms. The steady-state activation function was

$$m_\infty = \frac{1}{1+\exp[(V_m - V)/s_m]}, \tag{2}$$

with $V_m = -4$ mV and $s_m = 7$ mV (11). With regards to channel inactivation, some types of $Ca^{2+}$ channels are inactivated by $Ca^{2+}$, while others exhibit voltage-dependent inactivation. We found that fixed rate constants $k_-$=0.018 $ms^{-1}$ and $k_+$=0.0324 $ms^{-1}$ were sufficient to match inactivation experimentally observed in (11). The stochastic channel dynamics (1) was simulated as realizations of the discrete-state continuous-time Markov chain with transition probabilities for a small time step $\Delta t$ described by

$$\begin{bmatrix} O(t+\Delta t) \\ C(t+\Delta t) \\ B(t+\Delta t) \end{bmatrix} = \begin{bmatrix} 1-(\beta+k_+)\Delta t & \alpha\Delta t & k_-\Delta t \\ \beta\Delta t & 1-\alpha\Delta t & 0 \\ k_+\Delta t & 0 & 1-k_-\Delta t \end{bmatrix} \begin{bmatrix} O(t) \\ C(t) \\ B(t) \end{bmatrix}. \tag{3}$$

Monte Carlo simulations were performed and the single-channel open-state $O(t)$ was used to compute the single-channel current as

$$I_{sc}(t) = g_{sc} O(t)(V(t) - V_{Ca}) \tag{4}$$

where $g_{sc}$ is the single channel conductance. In the cluster case, the total current is simulated by summing 5 independent realizations of a single channel current ($I_{sc}$). Both the current driving force and open probability are coupled to the time-varying membrane potential $V(t)$. Specifically, the driving force decreases as $V(t)$ increases towards the $Ca^{2+}$ reversal potential $V_{Ca}$ whereas the open probability increases with $V(t)$.

ENDOGENOUS BUFFERS

In all simulations we assumed the presence of a single immobile endogenous $Ca^{2+}$ buffer, in agreement with Kits et al. (15), and no mobile buffers were considered. Binding of $Ca^{2+}$ to the buffers is described by simple mass action kinetics with one-to-one stoichiometry,

$$B + Ca^{2+} \underset{k_{off}}{\overset{k_{on}}{\rightleftharpoons}} CaB, \tag{5}$$

where $k_{on}$ and $k_{off}$ are association and disassociation rates, respectively. The reaction-diffusion equations for the $Ca^{2+}$ concentration and for the free unbound buffers are taken from (20):

$$\begin{aligned}\frac{\partial[Ca^{2+}]}{\partial t} = {} & D_{Ca}\nabla^2\left[Ca^{2+}\right] - k_{on}\left[Ca^{2+}\right][B] + k_{off}\left(B_{total} - [B]\right) + \frac{1}{2F} I_{sc}(t)\delta(r - R, \theta) \\ & - k_{uptake}\left(\left[Ca^{2+}\right] - \left[Ca^{2+}\right]_0\right),\end{aligned} \tag{6}$$

$$\frac{\partial[B]}{\partial t} = -k_{on}\left[Ca^{2+}\right][B] + k_{off}\left(B_{total} - [B]\right), \tag{7}$$

185 where $D_{Ca}$ is the diffusion coefficient for unbound $Ca^{2+}$. We chose $D_{Ca}$=0.2 μm$^2$ ms$^{-1}$ (1) and
186 assumed that the distribution of the immobile buffer is spatially uniform. The second-to-last term
187 in Eq. 6 represents $Ca^{2+}$ influx, where $F$ is Faraday's constant, $I_{sc}(t)$ is the (inward) single-
188 channel (or 5-channel-cluster) calcium current, and $\delta(r\text{-}R,\theta)$ is the Dirac delta function centered
189 at $r$=$R$ and $\theta$=0 (i.e., at the center of the base of the cone). The last term defines net $Ca^{2+}$ uptake
190 into internal stores such as the endoplasmic reticulum with constant rate $k_{uptake}$ =0.3 μM/ms$^{-1}$.
191 $[Ca^{2+}]_0$ is the $Ca^{2+}$ concentration in case of no $Ca^{2+}$ influx and spatiotemporal equilibrium. In
192 accordance with simulation studies performed by Kits et al. (16) in melanotroph cells, we set the
193 endogenous buffer parameters $k_{on}$=0.1 μM$^{-1}$ ms$^{-1}$, $K_D$= $k_{off}/k_{on}$ =10 μM, and $B_{total}$=900 μM. No-
194 flux boundary conditions hold for $Ca^{2+}$ at all boundaries. The reaction-diffusion equations were
195 solved using the Calcium Calculator (CalC) software developed by Victor Matveev (21). CalC
196 uses an alternating-direction implicit finite difference method, with second order accuracy in
197 space and time, and with adaptive time steps.

198 EXOCYTOSIS MODEL

199 We initially used a 6-pool exocytosis model (4), which describes the fraction of granules
200 in various pools of granules described as docked, primed, domain bound, or in one of three pre-
201 fusion states distinguished by the number of bound $Ca^{2+}$ ions. However, for the relatively short
202 time courses used here (5 sec), our preliminary simulations showed no significant differences
203 between this 6-pool model and a simpler 4-pool model in which the docked, primed, and domain
204 bound pools were combined into a single pool that we call the "primed" pool. We use this
205 simplified model (Fig. 2), which is similar to a model of exocytosis in melanotroph cells (16) in
206 all simulations. Here, the granule can be in one of four different states: a primed state where the
207 granule is adjacent to the plasma membrane ($N_0$), or states in which one ($N_1$), two ($N_2$), or three
208 ($N_3$) $Ca^{2+}$ ions are bound to the $Ca^{2+}$ sensor, likely synaptotagmin (31). Once in state $N_3$ the
209 granule fuses with the membrane and releases its hormone content at rate $u_1$. Granule release is
210 triggered by local $Ca^{2+}$ levels ($C_{loc}$), as indicated in Fig. 2, while resupply is dependent on the
211 bulk calcium concentration $C_i$, which is computed as the submembrane $Ca^{2+}$ concentration 1.5
212 μm from the channel. The rate of resupply per cell $r_1$ is

213

$$r_1 = \frac{C_i(t) r_1^0}{C_i(t) + K_p}, \tag{8}$$

with $K_p$ =2.3 μM (4, 40), and $r_1^0$ is the maximal resupply rate per cell.

All secretion model steps are assumed to be reversible, except for fusion. The local $Ca^{2+}$ concentration was determined by solving the $Ca^{2+}$ reaction-diffusion equations and using the $Ca^{2+}$ value at the release site (Eqs. 6,7). The exocytosis model describing release per cell is given by the following differential equations:

$$\begin{aligned}
\frac{dN_0}{dt} &= -\left(3k_1 C_{loc}(t) + r_{-1}\right) N_0 + r_1(C_i(t)) + k_{-1} N_1, \\
\frac{dN_1}{dt} &= -\left(2k_1 C_{loc}(t) + k_{-1}\right) N_1 + 3k_1 C_{loc}(t) N_0 + 2k_{-1} N_2, \\
\frac{dN_2}{dt} &= -\left(k_1 C_{loc}(t) + 2k_{-1}\right) N_2 + 2k_1 C_{loc}(t) N_1 + 3k_{-1} N_3, \\
\frac{dN_3}{dt} &= -\left(u_1 + 3k_{-1}\right) N_3 + k_1 C_{loc}(t) N_2,
\end{aligned} \tag{9}$$

where $N_i$ is the number of granules in pool $i$. Experimental data (37) indicate a relatively low $Ca^{2+}$ binding affinity; as a consequence, we use the $Ca^{2+}$ affinity value $k_d = k_{-1}/k_1$=27 μM in Eqs. 9.

We used two sets of initial conditions for the granule/exocytosis model. In the model of Chen et al. (4) the number of primed granules (pool $N_0$) is equal to 40 per cell. Hence, we set as initial condition $N_0$=40 primed granules, each a fixed distance from a single channel (so 35 channels are not associated with granules). Assuming that – in any one simulation – all $Ca^{2+}$ channels in the cell behave identically according to the Markov simulation, the granules will be exposed to the same $Ca^{2+}$ profile. To calculate average cellular exocytosis, we performed 10 (single channel) or 5 (cluster) simulations and computed average values of $N_i$ at each time point.

This initial condition ($N_0$=40) reflects experiments such as single-cell capacitance measurements of triggered exocytosis, where no exocytosis is occurring before the experiment (36, 37). For

interpreting hormone secretion experiments, where secretion is ongoing, the steady state of the model is more relevant. We found that the pools empty within seconds (see Results), and therefore considered initial conditions where all pools are empty to reflect secretion experiments.

The exocytosis rate per cell, with $N_3$ the average of 10 or 5 trials as explained above, is

$$J_F(t) = u_1 N_3(t), \tag{10}$$

and the cumulative number of fused granules per cell is

$$M_F(t) = \int_0^t u_1 N_3(t')dt'. \tag{11}$$

To show how much of the simulated secretion is due to increased $Ca^{2+}$ influx during bursting compared to spiking electrical activity, that is, to investigate whether bursting increases the $Ca^{2+}$-current sensitivity of exocytosis (26), we related exocytosis to the total charge entering via the $Ca^{2+}$ channel or channel cluster (26):

$$Q(t) = \int_0^t I_{sc} ds. \tag{12}$$

The exocytosis model was solved using the MATLAB (R2012b, The MathWorks®) function ode15s.

[Figure 2]

244 **RESULTS**

245 *Secretion evoked by $Ca^{2+}$ influx through single channels is increased when converting spiking to*
246 *bursting electrical activity through dynamic clamp*

247 Gonadotrophs release little LH under basal conditions, which has been suggested to be
248 associated to their typical spiking electrical behavior (10). We have previously shown that
249 adding a BK-type $K^+$ current to a spiking gonadotroph can change its behavior into bursting (35).
250 Figure 3 shows an example of such a cell where the injected BK-type current induces bursting in
251 an otherwise spiking gonadotroph. We also show the average of 10 independent simulations,
252 each with a stochastic $Ca^{2+}$ channel providing $Ca^{2+}$ to the interior of the cell and subsequent $Ca^{2+}$
253 diffusion. The $Ca^{2+}$ model is driven by either the spiking voltage pattern (left) or the bursting
254 pattern (right) obtained by injecting a BK-type $K^+$ current via dynamic clamp. Average $Ca^{2+}$
255 profiles are reported at distances of 30, 200, and 1500 nm from the $Ca^{2+}$ channel. As expected,
256 close to the channel, i.e., 30 nm, $Ca^{2+}$ reaches high concentrations of some tens of micromolar on
257 average with peaks up to ~70 μM during spiking activity and ~110 μM during bursting. The
258 traces are very noisy due to the stochastic openings of the $Ca^{2+}$ channel. The average $Ca^{2+}$
259 concentration decreases with distance from the channel, reaching less than 1 μM at a distance of
260 1500 nm. In addition, the noise is attenuated due to the effects of diffusion, which acts as a low-
261 pass filter. $Ca^{2+}$ measurements using a fluorescent dye such as fura-2 report on the $Ca^{2+}$
262 concentration averaged over the cell, and have time courses similar to those shown in the bottom
263 row of Fig. 3 (30, 32).

264 [Figure 3]

265

266 We now locate the exocytosis machinery at different distances from the $Ca^{2+}$ channel and
267 use the $Ca^{2+}$ concentration at that location to drive the exocytosis model (Fig. 2 and Eqs. 9).
268 Figure 4 shows the average number of fused granules over time at different distances. If the
269 release site is 30 nm from the channel, it is exposed to very high $Ca^{2+}$ concentrations, whether
270 the cell is spiking or bursting, and exocytosis occurs at its maximum rate that releases all the
271 granules in the primed pool $N_0$ (40 granules) very soon after the start of the input train. A similar

272 result occurs if the release site is located 100 nm from the channel. Thus, if the release site and
273 channel are within 100 nm of each other it does not matter whether the cell is spiking or bursting,
274 the secretion level will be the same, since the $Ca^{2+}$ concentrations at the exocytotic machinery
275 are in both cases saturating. At a distance of 200 nm there is a difference between exocytosis
276 evoked by spiking and that evoked by bursting; the bursting pattern (solid) evokes release at a
277 higher rate than the spiking pattern (dashed), though both release almost all available granules by
278 the end of the 5 second input train. The advantage of bursting over spiking is amplified when the
279 release site is situated further from the channel, at 300 nm or 500 nm. Even though the absolute
280 number of fused granules is lower when the channel and the release site are more distant, the
281 bursting voltage trace releases more granules than the spiking trace at all time points. Thus, our
282 simulations support the notion that adding an outward $K^+$ current can, by changing spiking to
283 bursting activity, increase secretion (6, 29).

284 These observations imply that the primed pool of granules can be emptied very quickly,
285 and this fusion process is likely monitored with capacitance measurements of exocytosis that
286 take place over a short period of time (14). In our data, the spiking voltage trace shows 5 spikes
287 in 5 seconds, each spike lasting ~40 ms (Fig. 3Ai). On average, each 40 ms depolarization of a
288 pulse train was found to evoke ~10 fF of exocytosis (19). Thus, based on these experiments we
289 expect ~50 fF exocytosis during the 5 seconds in Fig. 3. In our simulations, exocytosis at a
290 distance of 200 nm from the channel is ~30 granules. If we assume that a single granule
291 corresponds to ~2fF (39, 42), we get a capacitance measurement of ~60 fF, close to the ~50 fF
292 calculated from (19).

293 [Figure 4]

294 However, most secretion measurements are made from a cell population over a period of
295 minutes or tens of minutes. In such measurements the resupply of the primed pool by the reserve
296 granule pool is rate limiting. We next look at the effects of resupply by emptying the primed pool
297 $N_0$ at the beginning of the simulation and from this initial condition evaluate the differential
298 exocytosis evoked by spiking and bursting.

299 The cumulative number of fused granules as a function of time is shown in Fig. 5 (top
300 panel). Bursting evokes more release regardless of the distance between the channel and the

301 granule. This is in spite of the fact that at short distances the local $Ca^{2+}$ concentration saturates
302 the release site, and highlights the importance of the dependence of resupply on the global, rather
303 than local, $Ca^{2+}$ concentration. That is, the simulated global $Ca^{2+}$ concentration is higher during
304 bursting than during spiking, as measured by fluorescent dyes (22), and this results in a greater
305 rate of resupply in response to bursting. When the channel is close to the release site all granules
306 becoming available due to the resupply are fused almost immediately, so resupply is rate
307 limiting. Farther than 200 nm from the channel, local $Ca^{2+}$ concentrations start to play a
308 predominant role since the exocytosis machinery is no longer saturated, and therefore differences
309 in local $Ca^{2+}$ levels as well as global levels are responsible for differences in the exocytosis rates.

310 [Figure 5]

311 There are two factors that could contribute to the greater effectiveness of bursting at
312 evoking secretion in the model. One is that bursting brings in more $Ca^{2+}$ over the 5 seconds of
313 simulation time, increasing resupply rate relative to spiking, as mentioned above. The other is
314 that the dynamics of $Ca^{2+}$ diffusion and the exocytotic machinery favor the bursting signal over
315 the spiking signal. That is, bursting is more efficient than spiking at evoking release. To test the
316 latter, we plot the number of fused granules versus the total $Ca^{2+}$ entry $Q$ (Fig. 5, bottom panels).
317 For release sites closer than 200 nm from the channel the efficiencies of the spiking and bursting
318 patterns are virtually the same. It is only at distances of 200 nm or greater that bursting becomes
319 more efficient than spiking, since at these distances the number of fused granules per total $Ca^{2+}$
320 entry is larger when the cell is bursting. This is due to the longer duration of the bursting events,
321 which produce longer-duration $Ca^{2+}$ signals that are advantageous for the exocytosis machinery
322 that requires the binding of three $Ca^{2+}$ ions to evoke granule fusion. In fact, in simulations in
323 which only two $Ca^{2+}$ ions are needed to evoke fusion the efficiencies of spiking and bursting are
324 the same at a 200 nm distance, and bursting is only slightly more efficient at 300 and 500 nm
325 distances (not shown).

326 As a final quantification of the effectiveness of bursting vs. spiking at evoking secretion
327 we show the ratio between bursting-evoked secretion and spiking-evoked secretion in Fig. 6
328 (solid line). This ratio is calculated from the total number of fused granules at the end of the 5-
329 sec input voltage train as a function of distance between the channel and the release site. Up until

330 a distance of 100 nm the ratio is ~1.5; the burst pattern evokes a slightly higher amount of
331 secretion than spiking. Past this distance the ratio increases continuously, reaching a value of
332 ~8.5 at a distance of 700 nm. Thus, there is between 1.5 and 8.5 times more secretion by the end
333 of the 5-sec stimulation with bursting versus spiking. Plotting the ratio of exocytosis during
334 spiking and bursting but normalized to the charge *Q* (Fig. 6, dashed line) shows that spiking and
335 bursting have almost the same $Ca^{2+}$ current sensitivity close to the channel (i.e., they are equally
336 efficient at evoking release), but farther away bursting becomes more efficient than spiking,
337 reaching a 5.5-fold higher $Ca^{2+}$ current sensitivity at a distance of 700 nm from the channel.

338 In summary, our simulations suggest that LH secretion from a gonadotroph could
339 increase substantially if the electrical pattern switched from spiking to bursting, for example
340 because of the addition of a BK-type current.

341 [Figure 6]

342 *Secretion evoked by $Ca^{2+}$ influx through a cluster of channels*

343 The previous simulations assumed that each release site is acted upon by $Ca^{2+}$ from single
344 channels, and indeed there is evidence supporting this, in both endocrine cells and in neuronal
345 synapses (11, 17). However, it is likely that hormone release sites receive $Ca^{2+}$ from several
346 channels, and there is also evidence for this (2, 3). In the next set of simulations we consider
347 such a situation, where a release site is affected by $Ca^{2+}$ from a cluster of 5 stochastic $Ca^{2+}$
348 channels. For simplicity we assume that these are equidistant from the release site.

349 Figure 7 shows the $Ca^{2+}$ concentration at different distances from the channel cluster in response
350 to the spiking or bursting voltage trace. Close to the cluster (30 nm), $Ca^{2+}$ rises to a level of
351 several hundreds of micromolar, about five times larger than in the single-channel case. At
352 greater distances, the increase over the single-channel level is less, since now the different
353 clusters are 6600 nm apart so that a release site located 1500 nm from a cluster is >5000 nm from
354 the next nearest cluster. In contrast, with uniform distribution of the same number of channels
355 (the single channel case), a release site located 1500 nm from one channel was located the same
356 distance from a second channel, so it received an equal amount of $Ca^{2+}$ from both. Hence,
357 whereas a cluster of 5 channels provides ~5 times higher $Ca^{2+}$ levels to granules located close to

358 the channels, a granule located 1500 nm from channels will be exposed to just ~5/2=2.5 times
359 higher $Ca^{2+}$ concentrations in the case of channel clusters compared to the single-channel
360 configuration.

361 [Figure 7]

362 Figure 8 (upper panels) shows that bursting is always superior to spiking in evoking exocytosis
363 when channels are in clusters and the primed pool is initially empty. In contrast, the difference in
364 $Ca^{2+}$ current sensitivity is hardly observable when the release site is less than 300 nm from the
365 channel cluster (Fig. 8, lower panels). It is therefore mostly the larger amount of $Ca^{2+}$ entering
366 during bursting that determines the difference in secretion. Figure 9 summarizes the results for
367 channel clusters. Even at the closest release site/cluster distances the bursting-to-spiking ratio of
368 the total number of fused granules is ~1.5, and increases to ~4.5 at 700 nm (solid line). The
369 relative efficiency, i.e., the bursting-to-spiking ratio of the total number of granules normalized
370 to $Ca^{2+}$ entry, is ~1 up to 300 nm, and increases then to ~2.5 at 700 nm. Thus, just as with single-
371 channel-evoked release, bursting provides more secretion than does spiking when exocytosis is
372 triggered by channel clusters. However, the advantage of bursting over spiking becomes manifest
373 at greater distances for clusters than for single channels, 100 nm in Fig. 6 vs. 300 nm in Fig. 9..
374 Because the trends are qualitatively similar with single-channel and cluster-evoked secretion, we
375 focus on only one type (single-channel secretion) in the remaining simulations.

376 [Figure 8]

377 [Figure 9]

378 *Bursting superiority depends on the frequency of spiking*

379 As a second example, we now use recordings from a GH4 cell line. It has previously been
380 shown that pseudo-plateau bursting in some pituitary cells converts to spiking when BK-type $K^+$
381 channels are pharmacologically blocked, reducing the bulk $Ca^{2+}$ concentration (8). Does this
382 manipulation also result in a decrease of the domain $Ca^{2+}$ and therefore in decreased secretion?
383 We have shown that bursting can be rescued by adding BK current back to the cell using the
384 dynamic clamp technique (here and in (34)). In Fig. 10 we use both procedures. We begin with a
385 bursting lacto-somatroph GH4C1 cell (left column), then convert it to a spiking cell by the

386 addition of the BK channel blocker iberiotoxin (middle column), and finally convert the spiking
387 cell back to a bursting cell using dynamic clamp to inject a model BK current (right column). For
388 each case we calculate the $Ca^{2+}$ concentration at varying distances from the single stochastic
389 channel, as in prior simulations. Close to the channel, the $Ca^{2+}$ concentration is about the same
390 for all three voltage traces. However, at the greater distances, 1500 nm, the $Ca^{2+}$ levels
391 corresponding to the bursting voltage traces are higher than those corresponding to the spiking
392 voltage trace, as has been observed in experiments (18).

393 We next use these $Ca^{2+}$ time courses to simulate exocytosis for release sites located at
394 different distances from the $Ca^{2+}$ channel (Fig. 11). The results are summarized in Fig. 12, where
395 we show the number of fused granules evoked by the dynamic clamp-induced bursting vs. that
396 evoked by the spiking trace (solid black curve). In both cases, the ratio is near 1 up until a
397 separation distance of ~150-200 nm. At greater separations the ratio increases, indicating that at
398 these greater distances the bursting trace is more effective at evoking exocytosis than the spiking
399 trace. Normalizing to $Ca^{2+}$ influx reveals that the ratio of $Ca^{2+}$ current sensitivity is higher for
400 spiking close to the channel (ratio $< 1$) whereas bursting is more efficient farther from the
401 channel (Fig. 12). The fact that bursting is less superior to spiking after normalizing to $Ca^{2+}$
402 influx compared to the previous simulations of exocytosis using the traces from a gonadotroph
403 (Figs. 5 and 6) can be explained by noticing that, for this example, iberiotoxin-induced spiking
404 (Fig. 10B) occurs at a much higher rate (~1.8 Hz) than bursting (~0.8 Hz) (Fig 10A, C). Thus,
405 the dynamics of $Ca^{2+}$ entry is important for the control of exocytosis in addition to the number of
406 $Ca^{2+}$ ions entering the cell.

407 [Figure 10]

408 [Figure 11]

409 [Figure 12]

410

411 **DISCUSSION**

412 In the absence of hypothalamic stimulation or inhibition, pituitary lactotrophs and
413 somatotrophs release prolactin and growth hormone, while gonadotrophs comparatively secrete a
414 negligible amount of luteinizing hormone. This difference in basal hormone release was matched
415 by differences in spontaneous electrical activity between these cell types: lactotrophs and
416 somatotrophs often exhibit "pseudo-plateau" bursts of activity, causing periodic $Ca^{2+}$ influx,
417 while gonadotrophs usually produce spikes that are too brief to perturb the bulk $Ca^{2+}$ level
418 substantially (9). Such differences in the bulk $Ca^{2+}$ profiles lead to the hypothesis that different
419 patterns of spontaneous electrical activity result in different rates of hormone release. Bursting
420 causes hormone release from lactotrophs and somatotrophs, while spiking causes no hormone
421 release from gonadotrophs.

422 We tested this hypothesis in this paper. While $Ca^{2+}$ triggers hormone release and bursting
423 creates larger amplitude oscillations of average intracellular $Ca^{2+}$ than spiking, this does not
424 necessarily mean that bursting is more effective at triggering hormone release. The $Ca^{2+}$
425 concentration that matters is that seen by the hormone-containing granules at their release sites,
426 and if the release sites are close to $Ca^{2+}$ channels, the high $Ca^{2+}$ concentration in the
427 microdomains around the channels created by a single spike may be just as effective as that due
428 to a burst in triggering fusion of granules. Indeed, we found that spiking is as effective as
429 bursting in releasing a full pool of primed granules, as long as the release site is within 100 nm
430 from the channel (Fig. 4). However, if the primed pool of granules is initially empty, or if the
431 release site is located more than 100 nm from the channel, we found that bursting was always
432 more effective than spiking in triggering granule fusion.

433 There are two mechanisms for this difference between bursting and spiking. The first
434 results from the larger entry of $Ca^{2+}$ caused by bursting over spiking. Because the fraction of
435 open $Ca^{2+}$ channels is increased for a longer period of time during a burst than during a spike, a
436 burst causes a larger increase in bulk $Ca^{2+}$. Since the replenishment of the primed pool of
437 granules depends on bulk $Ca^{2+}$, bursting causes a higher rate of granules priming, which in turn
438 results in a higher rate of granule fusion. This effect is independent of the microdomain $Ca^{2+}$
439 concentration, so bursting causes a higher rate of granule fusions even if the release site is 100
440 nm or less from the channel (Fig. 5 top panels). However, this mechanism relies on the fact that,

441 at similar event frequency, bursting means that the electric potential across the cell membrane
442 stays high (i.e., at levels where the cell $Ca^{2+}$ current is high) for a larger fraction of time than
443 spiking. If spiking frequency is increased relative to bursting frequency so that the total amount
444 of active time is the same, then bulk $Ca^{2+}$ will be similar and so will the priming rate. In that
445 sense, the bursting pattern is not more effective than the spiking pattern if the amount of activity
446 (and therefore $Ca^{2+}$ entry) is normalized.

447 Nevertheless, there is a second mechanism that makes bursting more effective than
448 spiking at triggering granule fusion, even if we normalize by the total amount of $Ca^{2+}$ entry.
449 Because three free $Ca^{2+}$ ions must bind to the release machinery to trigger fusion, fusion is
450 facilitated by a stable high local $Ca^{2+}$ level. This is more likely to happen during bursting than
451 spiking, since $Ca^{2+}$ influx can be maintained longer during a burst than during a spike. This
452 advantage of bursting can be observed when the release site is more than 100 nm away from the
453 channel (Fig. 5 bottom panels). Cells must quickly restore intracellular $Ca^{2+}$ to low levels using
454 ATP-driven pumps, so there is an energetic cost associated with the entry of each $Ca^{2+}$ ion. For
455 release sites far from the $Ca^{2+}$ channels, the bursting pattern of activity results in a more efficient
456 use of $Ca^{2+}$ ions than the spiking pattern.

457 This may not be true at higher spike frequencies. If we increase spike frequency the
458 interval between each increase in local $Ca^{2+}$ goes down, so the higher effectiveness of bursting
459 might only be observed for release sites further away from the channels. We see that for the BK
460 (endogenous or injected by dynamic clamp) vs. no BK (i.e., in the presense of iberiotoxin) case,
461 where the maximum $Ca^{2+}$ concentration reached at 200 nm (Fig. 10) is similar to what we saw in
462 Fig. 3, but the interspike interval is lower so $Ca^{2+}$ does not go back down for long – in that case
463 spiking is at least as efficient as bursting in evoking release, for release sites up to 500 nm away
464 from the channels (Fig. 11). Nevertheless, the bursting pattern caused by the presence of a BK
465 current evoked more granule fusion because of the high average bulk $Ca^{2+}$ during bursting,
466 which results in higher rate of replenishment of the primed granules.

467 There are many examples in endocrinology where the pattern of a signal plays an
468 important role. A well-known example is that the frequency of hypothalamic gonadotropin-
469 releasing hormone pulses determines the differential release of luteinizing and follicle-

470 stimulating hormone by gonadotrophs (41). Here we used a hybrid experimental/modeling
471 approach to show that the actual pattern of electrical activity can trigger different rates of
472 hormone release. Since the discovery that pituitary cells are electrically active 40 years ago,
473 researchers have wondered how pituitary cells tune electrical activity to regulate hormone release
474 (24). It has been argued that since hypothalamic factors act on a number of ion channels on
475 pituitary cell membranes, electrical activity provides numerous ways for the hypothalamus to
476 modulate pituitary hormone release. Some of these factors may even modulate the time constant
477 of BK channels to switch the electrical activity pattern from spiking to bursting (6). The present
478 work shows that this switch to bursting may improve the effect of hypothalamic stimulating
479 neurohormones in increasing pituitary hormone secretion.

480 In summary, our modeling results show that bursting is superior to spiking in evoking
481 pituitary hormone release, since it brings more $Ca^{2+}$ into the cell, thus augmenting both local and
482 global $Ca^{2+}$ levels, which in turn increases resupply of secretory granules and exocytosis. We
483 found further that channel clustering is advantageous to isolated channels in controlling
484 secretion. Our results have implications beyond pituitary secretion. For example, human
485 pancreatic beta-cells show rapid bursting resembling pituitary plateau bursting (23, 27), which
486 has been suggested to be advantageous for insulin secretion (25). Further, $Ca^{2+}$ channel
487 clustering in beta-cells has been suggested to be important for insulin exocytosis (2).

488

489 **GRANTS**

490 JT and RB were partially supported by grant DMS1220063 from the National Science
491 Foundation.

492

493 **DISCLOSURES**

494 No conflicts of interest, financial or otherwise, are declared by the authors.

495

496

497 **REFERENCES**


498 1. **Allbritton NL, Meyer T, Stryer L**. Range of messenger action of calcium ion and
499 inositol 1,4,5-trisphosphate. *Science* 258: 1812–5, 1992.

500 2. **Barg S, Ma X, Eliasson L, Galvanovskis J, Göpel SO, Obermüller S, Platzer J,**
501 **Renström E, Trus M, Atlas D, Striessnig J, Rorsman P**. Fast exocytosis with few
502 Ca(2+) channels in insulin-secreting mouse pancreatic B cells. *Biophys. J.* 81: 3308–23,
503 2001.

504 3. **Bertram R, Smith GD, Sherman A**. Modeling study of the effects of overlapping Ca2+
505 microdomains on neurotransmitter release. *Biophys. J.* 76: 735–50, 1999.

506 4. **Chen Y, Wang S, Sherman A**. Identifying the targets of the amplifying pathway for
507 insulin secretion in pancreatic beta-cells by kinetic modeling of granule exocytosis.
508 *Biophys. J.* 95: 2226–2241, 2008.

509 5. **Dubinsky JM, Oxford GS**. Ionic currents in two strains of rat anterior pituitary tumor
510 cells. *J. Gen. Physiol.* 83: 309–339, 1984.

511 6. **Duncan PJ, Sengul S, Tabak J, Ruth P, Bertram R, Shipston MJ**. Large conductance
512 Ca(2+) -activated K(+) channels (BK) promote secretagogue-induced transition from
513 spiking to bursting in murine anterior pituitary corticotrophs. *J. Physiol.* 593: 1197–1211,
514 2015.

515 7. **Freeman ME, Kanyicska B, Lerant A, Gyorgy N**. Prolactin: Structure , Function , and
516 Regulation of Secretion. *Physiol. Rev.* 80: 1523–1631, 2000.

517 8. **Van Goor F, Li Y-X, Stojilkovic SS**. Paradoxical Role of Large-Conductance Calcium-
518 Activated K+ (BK) Channels in Controlling Action Potential-Driven Ca2+ Entry in
519 Anterior Pituitary Cells. *J. Neurosci.* 21: 5902–5915, 2001.

520 9. **Van Goor F, Zivadinovic D, Martinez-Fuentes AJ, Stojilkovic SS**. Dependence of
521 pituitary hormone secretion on the pattern of spontaneus voltage-gated calcium influx.
522 Cell type-specific action potential secretion coupling. *J. Biol. Chem.* 276: 33840–33846,
523 2001.

524 10. **Van Goor F, Zivadinovic D, Stojilkovic SS**. Differential expression of ionic channels in
525 rat anterior pituitary cells. *Mol. Endocrinol.* 15: 1222–1236, 2001.

526 11. **Hagiwara S, Ohmori H**. Studies of single calcium channel currents in rat clonal pituitary
527 cells. *J. Physiol.* 336: 649–61, 1983.

528 12. **Hodgking AL, Huxley AF**. A quantitative description of membrane current and its
529 application to conduction and excitation in nerve. *J. Physiol.* 117: 500–44, 1952.

530 13. **Keja JA, Kits KS**. Single-channel properties of high- and low-voltage-activated calcium
531 channels in rat pituitary melanotropic cells. *J. Neurophysiol.* 71: 840–55, 1994.

532 14. **Kits KS, Mansvelder HD**. Regulation of exocytosis in neuroendocrine cells: Spatial
533 organization of channels and vesicles, stimulus-secretion coupling, calcium buffers and
534 modulation. *Brain Res. Rev.* 33: 78–94, 2000.

535 15. **Kits KS, de Vlieger T a, Kooi BW, Mansvelder HD**. Diffusion barriers limit the effect
536 of mobile calcium buffers on exocytosis of large dense cored vesicles. *Biophys. J.* 76:
537 1693–1705, 1999.

538 16. **Kits KS, de Vlieger T a, Kooi BW, Mansvelder HD**. Diffusion barriers limit the effect
539 of mobile calcium buffers on exocytosis of large dense cored vesicles. *Biophys. J.* 76:
540 1693–1705, 1999.

541 17. **Klingauf J, Neher E**. Modeling buffered Ca2+ diffusion near the membrane: implications
542 for secretion in neuroendocrine cells. *Biophys. J.* 72: 674–90, 1997.

543 18. **Li YX, Rinzel J, Vergara L, Stojilković SS**. Spontaneous electrical and calcium
544 oscillations in unstimulated pituitary gonadotrophs. *Biophys. J.* 69: 785–95, 1995.

545 19. **Mansvelder HD, Kits KS**. The relation of exocytosis and rapid endocytosis to calcium
546 entry evoked by short repetitive depolarizing pulses in rat melanotropic cells. *J. Neurosci.*
547 18: 81–92, 1998.

548 20. **Matveev V, Zucker RS, Sherman A**. Facilitation through buffer saturation: constraints
549 on endogenous buffering properties. *Biophys. J.* 86: 2691–2709, 2004.

550 21. **Matveev V**. CalC • The Calcium Calculator • Victor Matveev, NJIT.
551 https://web.njit.edu/~matveev/.

552 22. **Milescu LS, Yamanishi T, Ptak K, Mogri MZ, Smith JC**. Real-time kinetic modeling
553 of voltage-gated ion channels using dynamic clamp. *Biophys. J.* 95: 66–87, 2008.

554 23. **Misler S, Barnett DW, Gillis KD, Pressel DM**. Electrophysiology of stimulus-secretion
555 coupling in human beta-cells. *Diabetes* 41: 1221–8, 1992.

556 24. **Mollard P, Schlegel W**. Why are endocrine pituitary cells excitable? *Trends Endocrinol.*
557 *Metab.* 7: 361–365, 1996.

558 25. **Pedersen MG, Cortese G, Eliasson L**. Mathematical modeling and statistical analysis of
559 calcium-regulated insulin granule exocytosis in beta-cells from mice and humans. *Prog.*
560 *Biophys. Mol. Biol.* 107: 257–264, 2011.

561 26. **Pedersen MG**. On depolarization-evoked exocytosis as a function of calcium entry:
562 Possibilities and pitfalls. *Biophys. J.* 101: 793–802, 2011.

563 27. **Riz M, Braun M, Pedersen MG**. Mathematical modeling of heterogeneous
564 electrophysiological responses in human β-cells. *PLoS Comput. Biol.* 10: e1003389, 2014.

565 28. **Sherman A, Keizer J, Rinzel J**. Domain model for Ca2(+)-inactivation of Ca2+ channels
566 at low channel density. *Biophys. J.* 58: 985–95, 1990.

567 29. **Stojilkovic SS, Tabak J, Bertram R**. Ion channels and signaling in the pituitary gland.
568 *Endocr. Rev.* 31: 845–915, 2010.

569 30. **Stojilkovic SS, Zemkova H, Van Goor F**. Biophysical basis of pituitary cell type-
570 specific Ca2+ signaling-secretion coupling. *Trends Endocrinol. Metab.* 16: 152–9, 2005.

571 31. **Stojilkovic SS**. Ca2+-regulated exocytosis and SNARE function. *Trends Endocrinol.*
572 *Metab.* 16: 81–83, 2005.

573 32. **Stojilkovic SS**. Pituitary cell type-specific electrical activity, calcium signaling and
574 secretion. *Biol. Res.* 39: 403–423, 2006.

575 33. **Tabak J, Gonzalez-Iglesias AE, Toporikova N, Bertram R, Freeman ME**. Variations
576 in the response of pituitary lactotrophs to oxytocin during the rat estrous cycle.
577 *Endocrinology* 151: 1806–13, 2010.

578 34. **Tabak J, Tomaiuolo M, Gonzalez-Iglesias a. E, Milescu LS, Bertram R**. Fast-
579 Activating Voltage- and Calcium-Dependent Potassium (BK) Conductance Promotes
580 Bursting in Pituitary Cells: A Dynamic Clamp Study. *J. Neurosci.* 31: 16855–16863,
581 2011.

582 35. **Tashjian AH, Yasumura Y, Levine L, Sato GH, Parker ML**. Establishment of clonal
583 strains of rat pituitary tumor cells that secrete growth hormone. *Endocrinology* 82: 342–
584 52, 1968.

585 36. **Thomas P, Surprenant a, Almers W**. Cytosolic Ca2+, exocytosis, and endocytosis in
586 single melanotrophs of the rat pituitary. *Neuron* 5: 723–733, 1990.

587 37. **Thomas P, Wong JG, Lee a K, Almers W**. A low affinity Ca2+ receptor controls the
588 final steps in peptide secretion from pituitary melanotrophs. *Neuron* 11: 93–104, 1993.

589 38. **Tse A, Hille B**. GnRH-induced Ca2+ oscillations and rhythmic hyperpolarizations of
590 pituitary gonadotropes. *Science.* 255: 462–464, 1992.

591 39. **Vardjan N, Jorgačevski J, Stenovec M, Kreft M, Zorec R**. Compound exocytosis in
592 pituitary cells. *Ann. N. Y. Acad. Sci.* 1152: 63–75, 2009.

593 40. **Voets T**. Dissection of Three Ca2+-Dependent Steps Leading to Secretion in Chromaffin
594 Cells from Mouse Adrenal Slices. *Neuron* 28: 537–545, 2000.

595 41. **Wildt L, Häusler A, Marshall G, Hutchison JS, Plant TM, Belchetz PE, Knobil E**.
596 Frequency and amplitude of gonadotropin-releasing hormone stimulation and
597 gonadotropin secretion in the rhesus monkey. *Endocrinology* 109: 376–85, 1981.

598 42. **Zorec R, Sikdar SK, Mason WT**. Increased cytosolic calcium stimulates exocytosis in
599 bovine lactotrophs. Direct evidence from changes in membrane capacitance. *J. Gen.*
600 *Physiol.* 97: 473–497, 1991.

601

602

603 FIGURE CAPTIONS

604 Figure 1. Calcium diffusion characteristics in the model. a) Spherical cell model used in
605 simulations. The cell diameter is 13 μm. $Ca^{2+}$ diffusion and buffering are simulated in a conical
606 region of the sphere. The channel or channel cluster is located at the center of the cone base on
607 the surface of the sphere. The base radius in the single channel case is 1.5 μm and in the cluster
608 case 3.3 μm. b) Upper panel: submembrane $Ca^{2+}$ concentrations (color coded, in μM) as a
609 function of time and the distance to the channel (d, measured along the cone base as indicated in
610 panel a) during spiking electrical activity. Lower panel: $Ca^{2+}$ concentration at 500 nm from the
611 channel as function of time.

612 Figure 2. Kinetic scheme of the exocytosis model. The pool $N_0$ consists of granules primed for
613 fusion and its resupply depends on the bulk cytosolic $Ca^{2+}$ concentration $C_i$. Fusion occurs upon
614 $Ca^{2+}$ binding controlled by the local concentration of $Ca^{2+}$, $C_{loc}$. The pools $N_1$, $N_2$, $N_3$ correspond
615 to the three $Ca^{2+}$ bound states, and $u_1$ is the fusion rate.

616 Figure 3. $Ca^{2+}$ concentration at different distances from a single stochastic $Ca^{2+}$ channel on the
617 surface of a conical region (average of 10 independent trials). The $Ca^{2+}$ channel is placed at the
618 center of the cone base with radius 1.5 μm. The $Ca^{2+}$ concentration is determined using a
619 mathematical model, in response to actual spiking (A) and bursting (B) voltage traces from a
620 gonadotroph. The switch to bursting was obtained by injecting a model BK-current into a spiking
621 cell using the dynamic clamp technique.

622 Figure 4. Single channel exocytosis simulation results with $N_0$=40 primed granules as initial
623 condition. Number of fused granules (average of 10 simulations) during spiking (dashed curve)
624 and bursting (solid curve) electrical activity for different distances between the single $Ca^{2+}$
625 channel and a release site as a function of time.

626 Figure 5. Single channel exocytosis simulation results with all the pools initially empty. Top
627 panels (i) show the number of fused granules as a function of time, as in Fig. 4. Bottom panels
628 (ii) show the cumulative number of fused granules during 5 seconds of simulation as function of
629 the cumulative calcium entry $Q$. (A) granules located at 30 nm, (B) 100 nm, (C) 200 nm, (D) 300
630 nm, or (E) 500 nm from the channel.

631 Figure 6. Summary of single channel exocytosis results with all the pools initially empty. The
632 bursting-to-spiking ratio of the total number of fused granules during 5 seconds of electrical
633 activity (solid line) shows that bursting evokes more secretion at all distances. In contrast, the
634 bursting-to-spiking ratio of the total number of granules normalized to change entry *Q* (dashed
635 line) shows that the efficiency of spiking and bursting are comparable for release sites located
636 close to the channel, but that bursting has superior efficiency farther from the channel.

637 Figure 7. $Ca^{2+}$ concentrations for a cluster of 5 channels (average of 5 independent trials). The
638 $Ca^{2+}$ channel is placed at the center of the cone base with radius 3.3 μm. The $Ca^{2+}$ concentration
639 is determined using the mathematical model, in response to actual spiking (A) and dynamic-
640 clamp induced bursting (B) voltage traces from a gonadotroph (same traces as in Fig. 3).

641 Figure 8. Channel cluster exocytosis simulation results with all the pools initially empty. Top
642 panels (i) show the number of fused granules as a function of time, evoked by spiking (dashed
643 curve) or bursting (solid curve). Bottom panels (ii) show the cumulative number of fused
644 granules during 5 seconds of simulation as a function of the cumulative $Ca^{2+}$ entry *Q*. (A)
645 granules located at 30 nm, (B) 100 nm, (C) 200 nm, (D) 300 nm, or (E) 500 nm from the
646 channel.

647 Figure 9. Summary of channel cluster exocytosis results with all the pools initially empty. The
648 bursting-to-spiking ratio of the total number of fused granules during 5 seconds of electrical
649 activity (solid line) shows that bursting evokes more secretion at all distances. In contrast, the
650 bursting-to-spiking ratio of the total number of granules normalized to change entry *Q* (dashed
651 line) shows that the efficiency of spiking and bursting are comparable for release sites located
652 close to the channel cluster, but that bursting has superior efficiency farther away.

653 Figure 10. $Ca^{2+}$ concentration at different distances from a stochastic $Ca^{2+}$ channel on the surface
654 of a conical region (average of 10 independent trials). The $Ca^{2+}$ channel is placed at the center of
655 the cone base with radius 1.5 μm. (A) Bursting profile in control condition. (B) Spiking profile in
656 the presence of the BK channel blocker iberiotoxin. (C) Bursting profile in the presence of
657 iberiotoxin and when BK current is injected back using the dynamic clamp. Sub panels show the
658 experimentally recorded voltage profile (i), and simulated $Ca^{2+}$ concentrations at 30 nm (ii), 200
659 nm (iii), or 1500 nm (iv) from the channel.

660 Figure 11. Single channel exocytosis simulation results with all the pools initially empty for
661 dynamic clamp-induced bursting. Top panels (i) show the number of fused granules as a function
662 of time, evoked by a spiking voltage trace (gray dashed curves) and bursting induced by dynamic
663 clamp in the presence of iberiotoxin (black solid curves). Bottom panels (ii) show the
664 cumulative number of fused granules during 5 seconds of simulation as a function of the
665 cumulative $Ca^{2+}$ entry $Q$. (A) granules located at 30 nm, (B) 100 nm, (C) 200 nm, (D) 300 nm, or
666 (E) 500 nm from the channel.

667 Figure 12. Summary of exocytosis simulation results with all the pools initially empty during
668 BK-current block and dynamic clamp. The ratios of the total number of fused granules between
669 bursting that results from dynamic clamp application with iberiotoxin vs. spiking that results
670 from iberiotoxin alone (solid black curve). The ratios of the total number of fused granules
671 normalized to the charge entry $Q$ are given by the dashed curves.

672

Table 1. Default parameters of the $Ca^{2+}$ channel model, $Ca^{2+}$ diffusion simulations and exocytosis model.

| Parameter | Value | Unit |
|---|---|---|
| **Current Simulation** | | |
| $s_m$ | 7 | mV |
| $v_m$ | -4 | mV |
| $k_+$ | 0.0234 | $ms^{-1}$ |
| $k_-$ | 0.018 | $ms^{-1}$ |
| $g_{Ca}$ | 20 | pS |
| **Diffusion Simulation** | | |
| $D_{Ca}$ | 0.22 | $\mu m^2 s^{-1}$ |
| $B_{total}$ | 900 | μM |
| $K_D$ | 10 | μM |
| $k_{on}$ | 0.1 | $\mu M^{-1} ms^{-1}$ |
| $k_{off}$ | 1 | $ms^{-1}$ |
| $[Ca^{2+}]_0$ | 0.22 | μM |
| **Secretion Model** | | |
| $k_1$ | 3.7 | $\mu M^{-1} s^{-1}$ |
| $k_{-1}$ | 100 | $s^{-1}$ |
| $r_1^0$ | 3.6 | $s^{-1}$ |
| $K_p$ | 2.3 | μM |
| $r_{-1}$ | 0.001 | $s^{-1}$ |
| $u_1$ | 1000 | $s^{-1}$ |

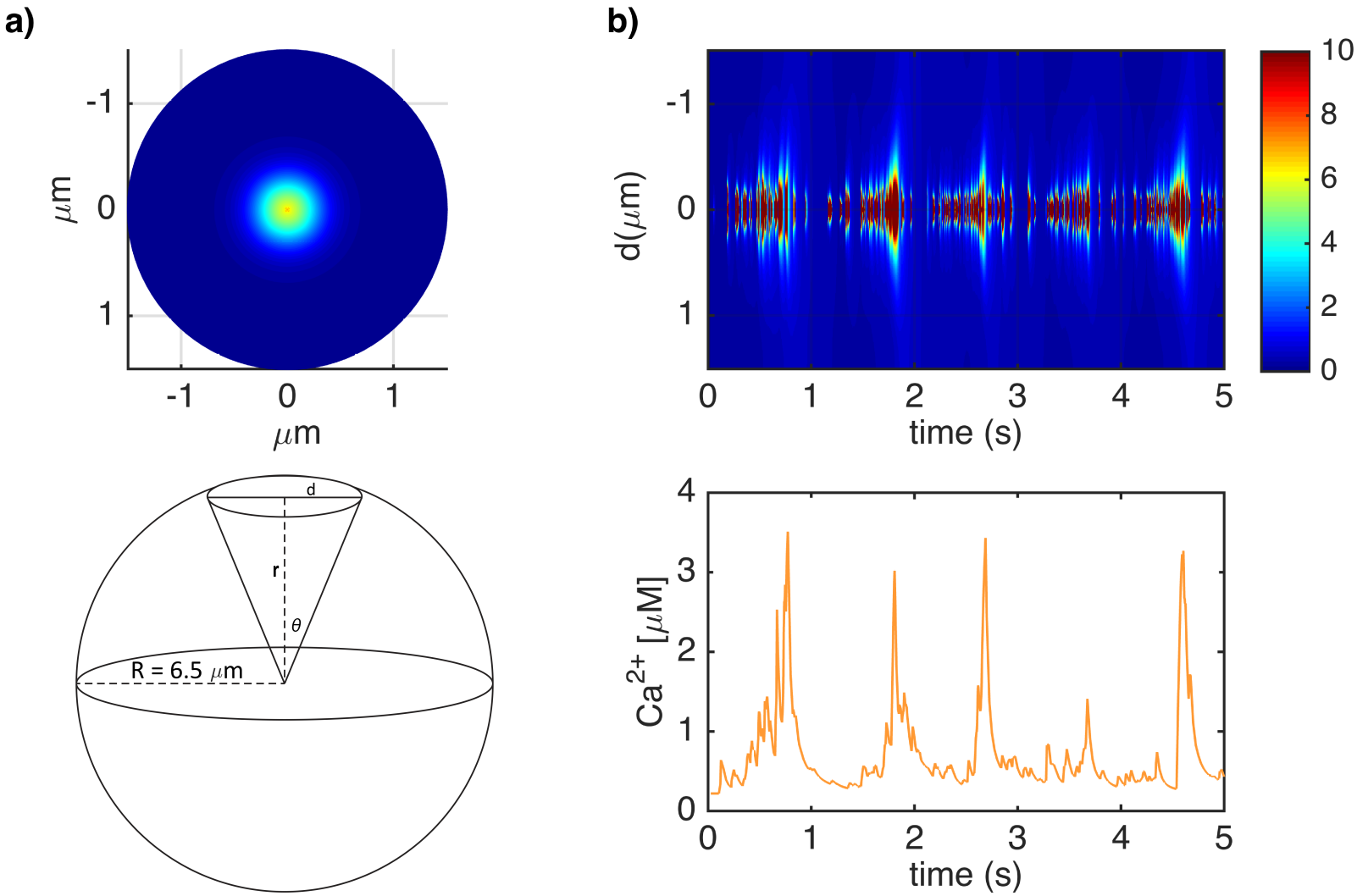
a)
b)
-1
0
1
μm
-1
0
1
μm
d
r
θ
R = 6.5 μm
-1
0
1
d(μm)
0
1
2
3
4
5
time (s)
10
8
6
4
2
0
4
3
2
1
0
Ca2+ [μM]
0
1
2
3
4
5
time (s)

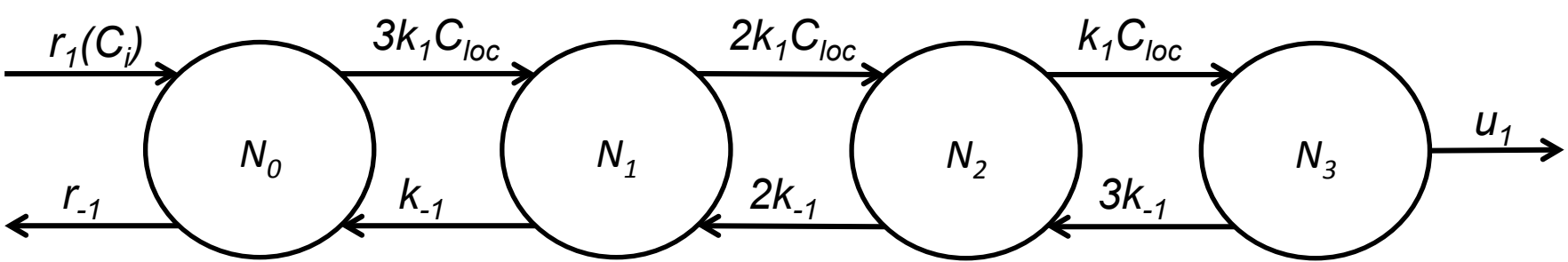
$r_1(C_i)$
$3k_1C_{loc}$
$2k_1C_{loc}$
$k_1C_{loc}$
$N_0$
$N_1$
$N_2$
$N_3$
$u_1$
$r_{-1}$
$k_{-1}$
$2k_{-1}$
$3k_{-1}$

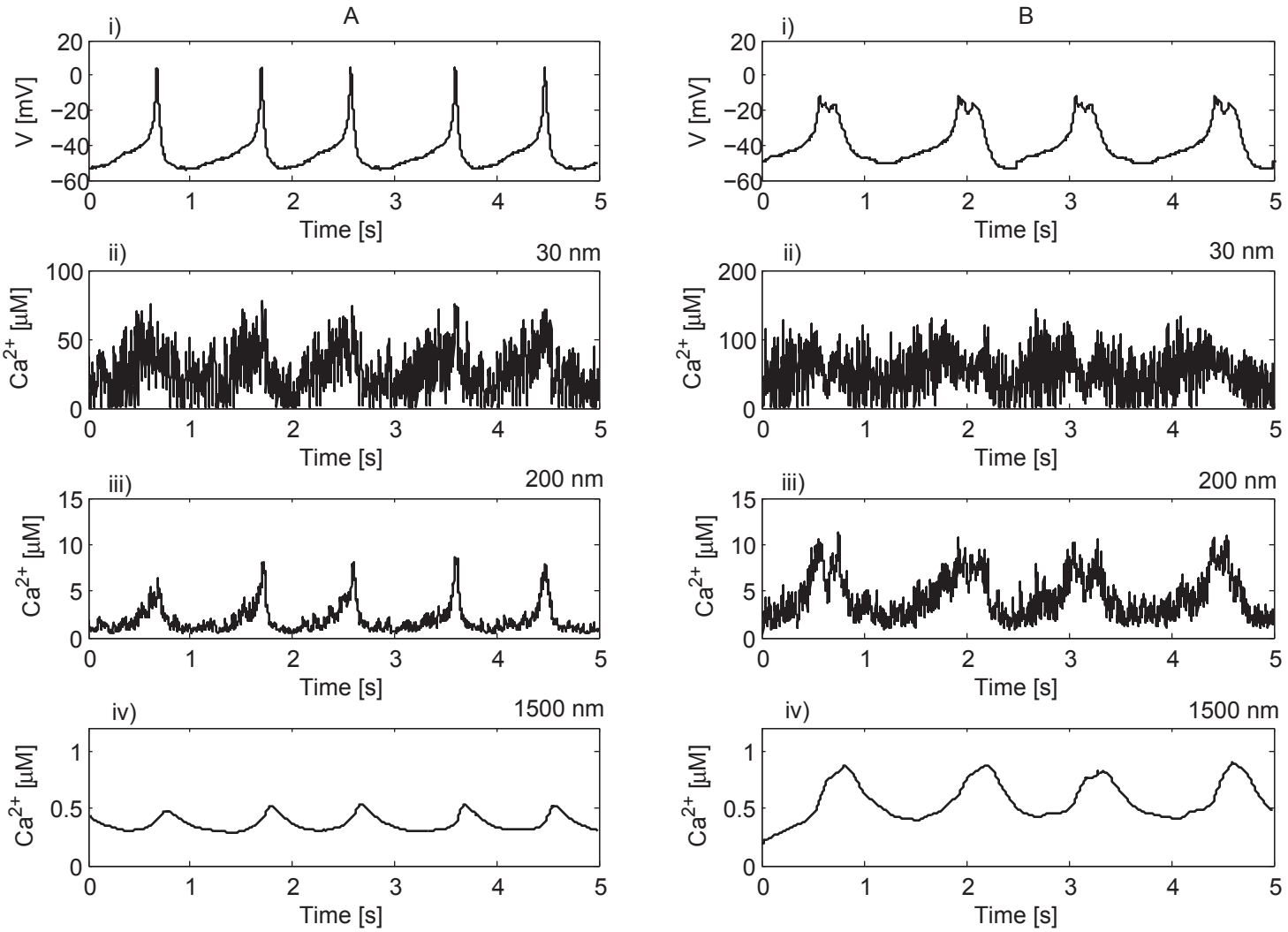
A
B
i)
ii)
iii)
iv)
30 nm
200 nm
1500 nm
V [mV]
Ca2+ [μM]
Time [s]

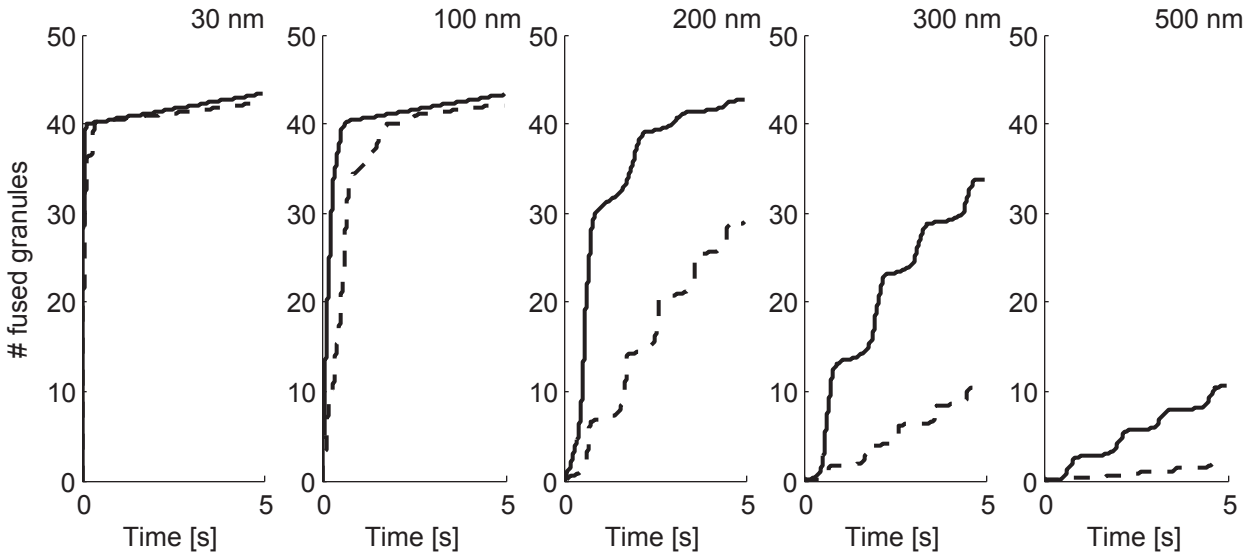
30 nm
100 nm
200 nm
300 nm
500 nm
# fused granules
Time [s]
0
10
20
30
40
50
5

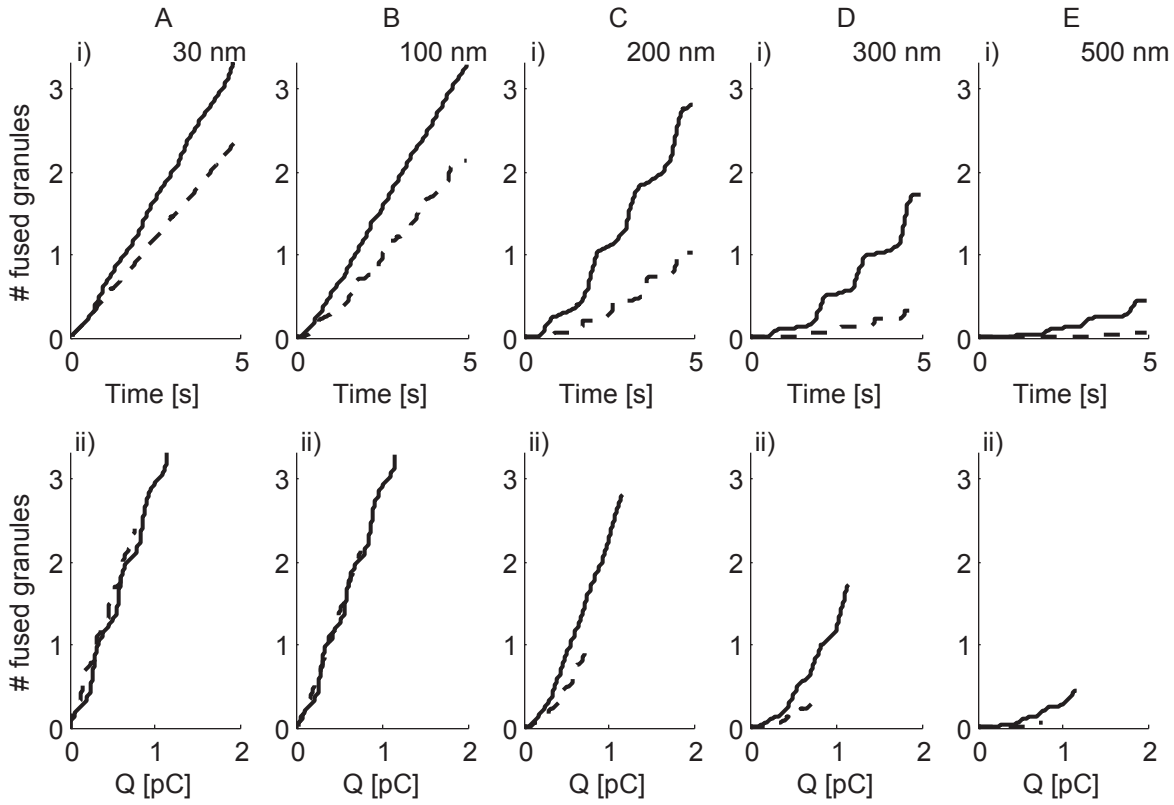
A
B
C
D
E
i)
30 nm
100 nm
200 nm
300 nm
500 nm
# fused granules
Time [s]
ii)
Q [pC]

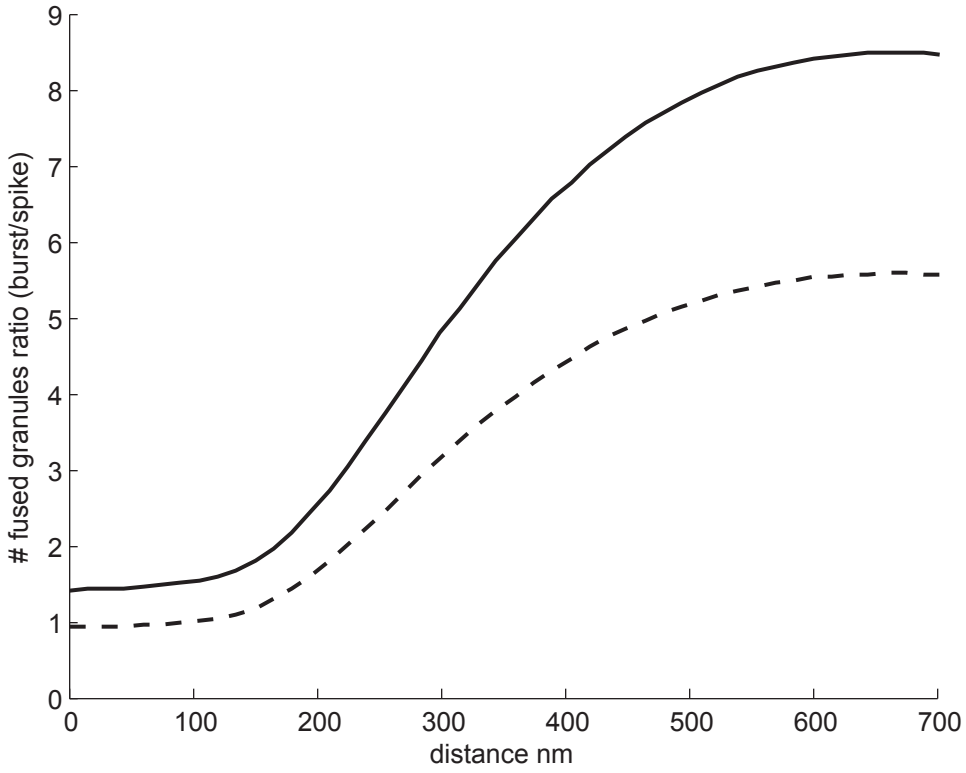
# fused granules ratio (burst/spike)
distance nm
0
1
2
3
4
5
6
7
8
9
0
100
200
300
400
500
600
700

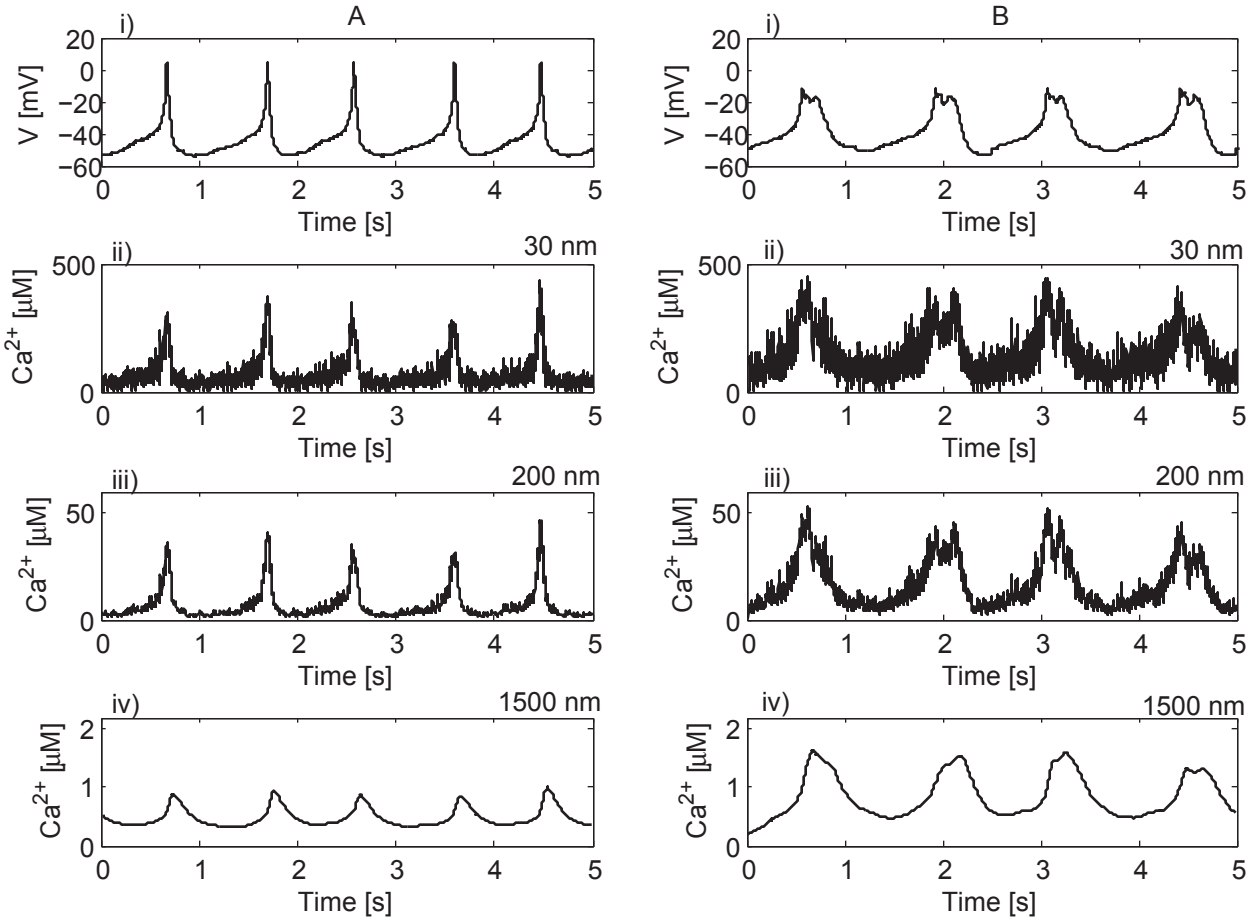
A
B
i)
ii)
iii)
iv)
30 nm
200 nm
1500 nm
V [mV]
Ca2+ [μM]
Time [s]

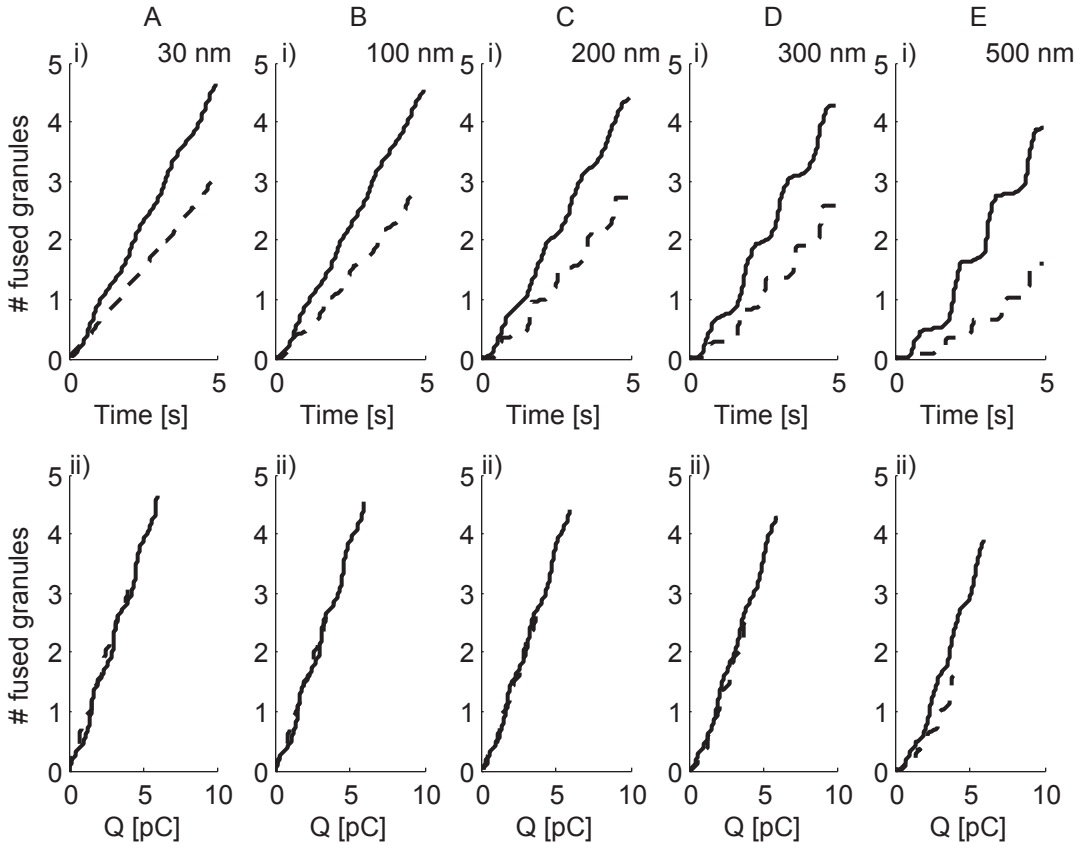
A
B
C
D
E
i)
30 nm
100 nm
200 nm
300 nm
500 nm
# fused granules
Time [s]
ii)
Q [pC]

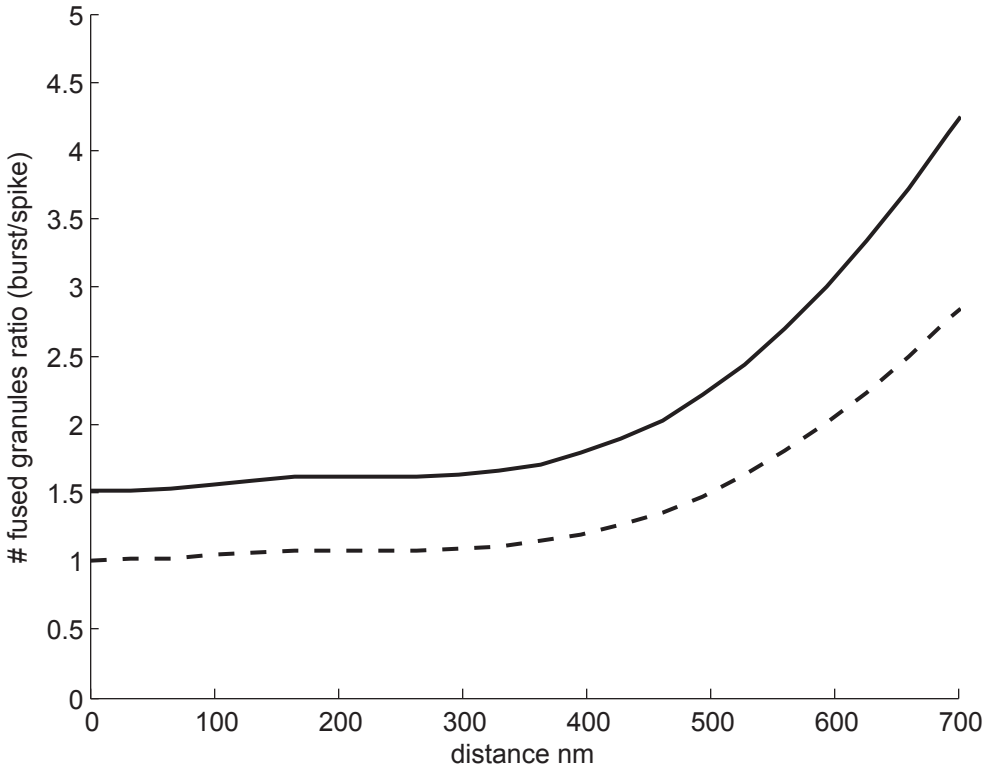
# fused granules ratio (burst/spike)
distance nm
0
0.5
1
1.5
2
2.5
3
3.5
4
4.5
5
0
100
200
300
400
500
600
700

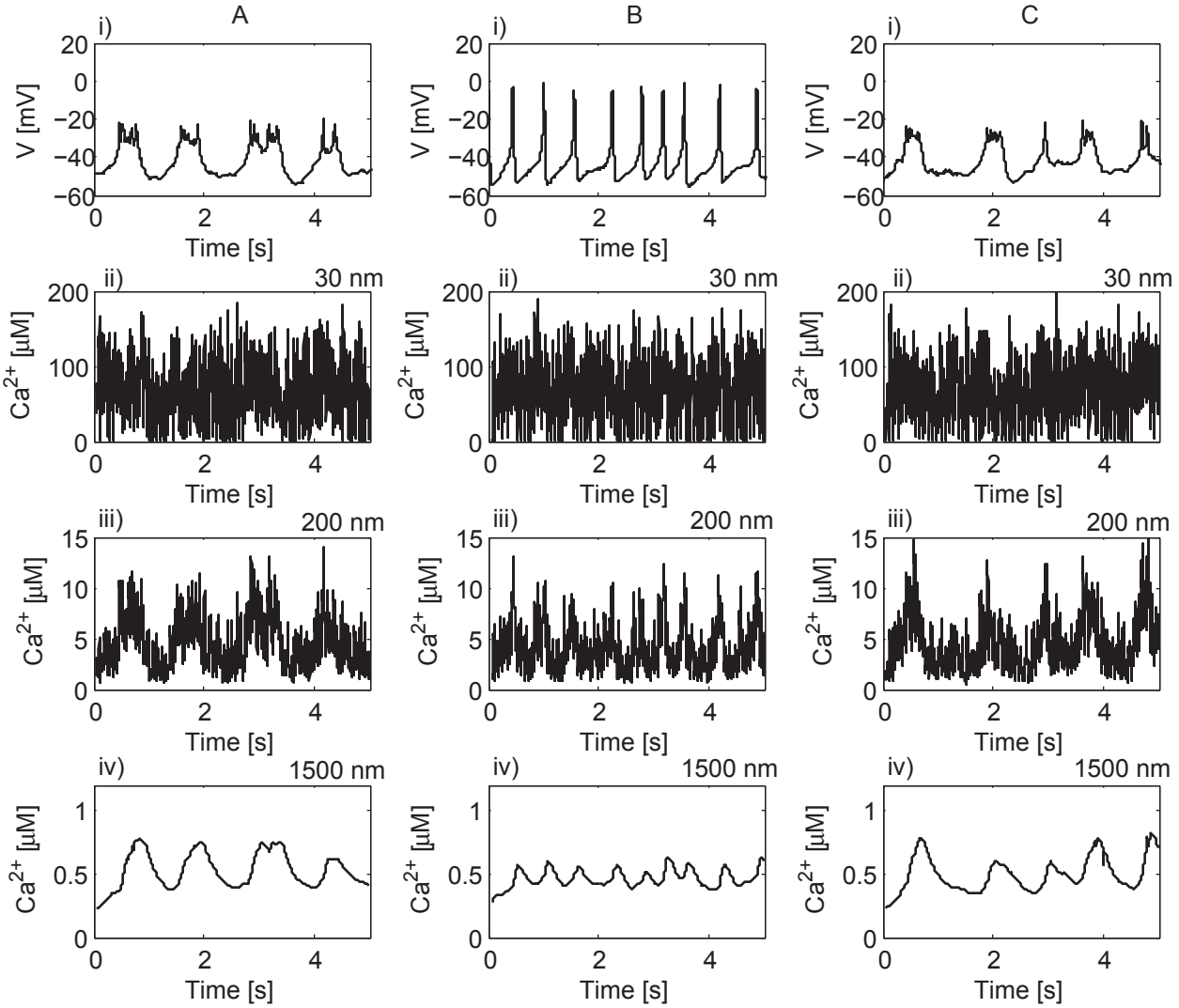
A
B
C
i)
ii)
iii)
iv)
30 nm
200 nm
1500 nm
V [mV]
Ca2+ [μM]
Time [s]

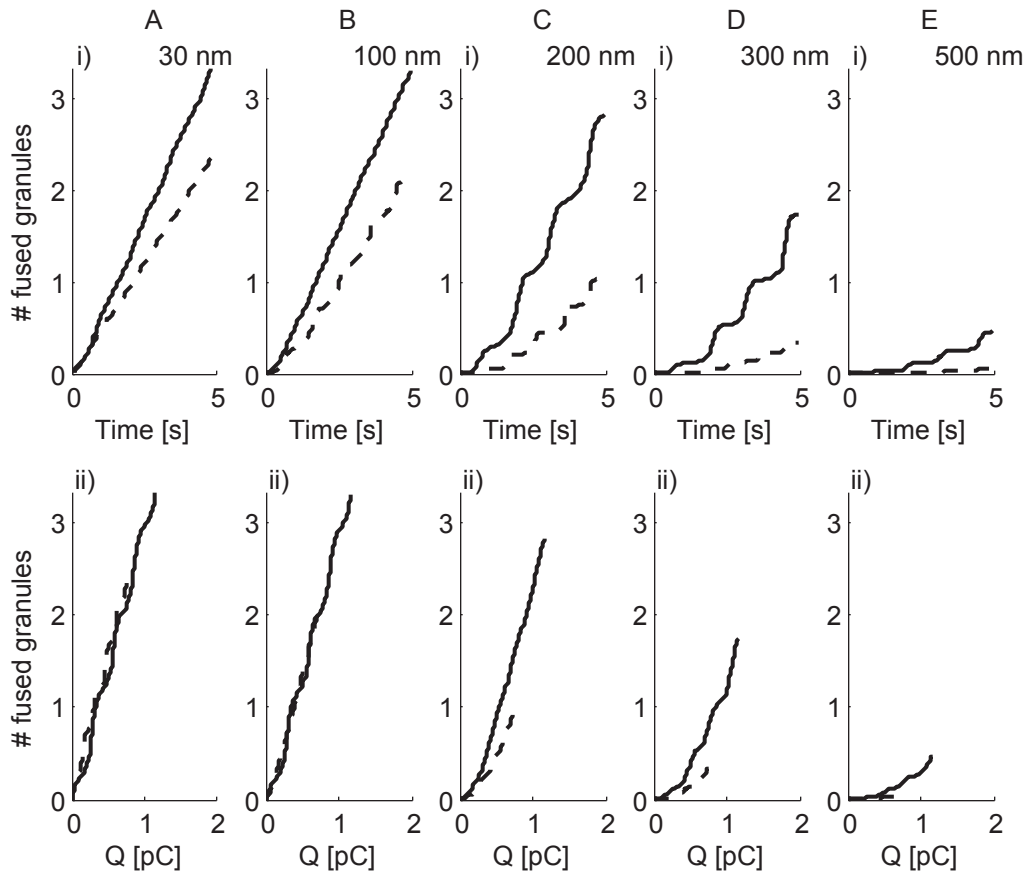
A
B
C
D
E
i)
30 nm
100 nm
200 nm
300 nm
500 nm
# fused granules
Time [s]
ii)
Q [pC]

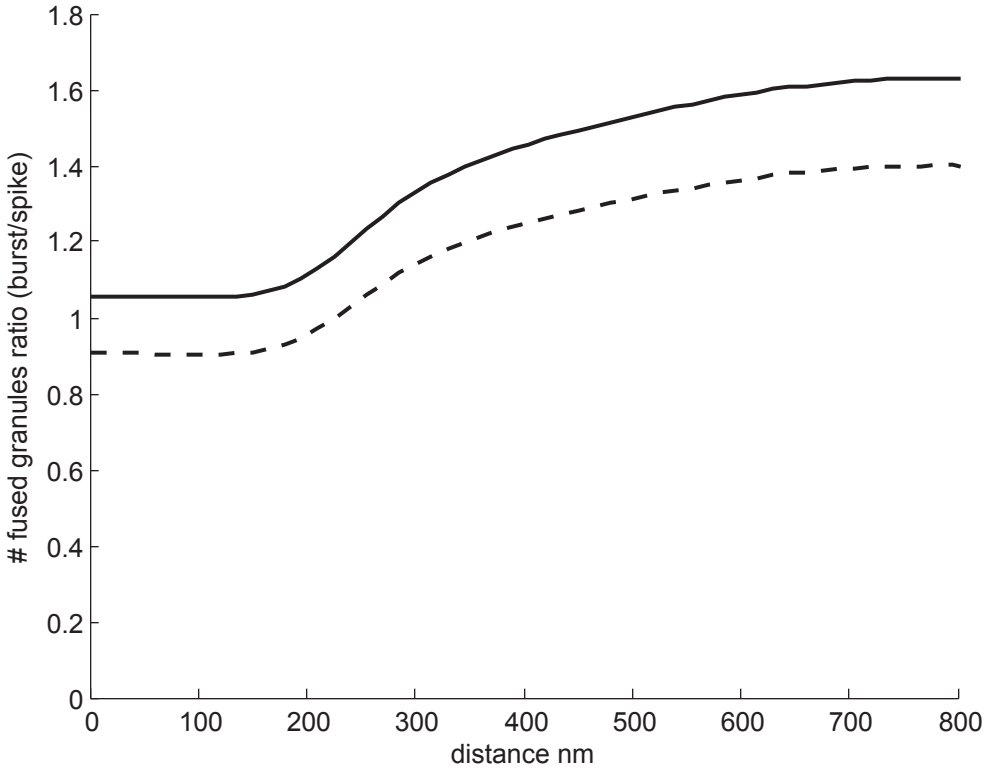
1.8
1.6
1.4
1.2
1
0.8
0.6
0.4
0.2
0
# fused granules ratio (burst/spike)
0
100
200
300
400
500
600
700
800
distance nm